AUT Journal of Mechanical Engineering

AUT J. Mech. Eng., 9(2) (2025) 179-194
DOI: 10.22060 /ajme.2025.23439.6135

# Kinetostatic and Dynamic Analyses of Micro-Positioning Compliant Mechanism Equipped with Piezoelectric Actuator

Ali Mojibi, Pouya Firuzy Rad, Hamed Ghafarirad *, Afshin Taghvaeipour

Department ofMechanical Engineering, Amirkabir University of Technology, Tehran, Iran

**ABSTRACT:** This paper proposes a compliant amplifying mechanism for micro-positioning applications by piezoelectric actuators. This mechanism has the advantage of being supported by both input and output ports, enhancing its out-of-plane stiffness, and making it more applicable for positioning devices. However, this property makes the mechanism more complicated for kinetostatic analyses. In this paper, analytical methods are presented to model the kinetostatic and dynamic behaviors. In addition, to take the nonlinear behavior into account, the hysteresis behavior of the mechanism and piezoelectric has been identified by the Prandtl-Ishlinski model. The results are validated by the finite element method (FEM) and experiments. The analytical method can estimate the amplification ratio, output stiffness and input stiffness of the mechanism with a deviation of approximately 9.5%, 20%, and 2%, respectively. Additionally, the resonant frequency obtained from the dynamic stiffness model is 394 Hz, which closely aligns with the results obtained from FEM simulation and experiments, i.e., 371 Hz and 365 Hz, respectively. Based on the conducted analyses, it can be concluded that the dynamic stiffness modeling results indicate a satisfactory correlation between the analytical and FEM method in terms of the amplification ratio and resonance frequency. Furthermore, the hysteresis identification model is appropriately linked with the experimental hysteresis loop with an RSME of less than 2μm for input signals with 1,2, and 4 second periods.

**Review History:**

Received: Aug. 19, 2024
Revised: Dec. 30, 2024
Accepted: Feb. 12, 2025
Available Online: Feb. 18, 2025

**Keywords:**

Compliant Mechanisms
Micro-positioning
Displacement Amplification
Kinetostatic
Dynamic Behavior

## 1- Introduction

Piezo actuators are renowned for their unique properties, including high precision and rapid response [1]. However, it is well-established that piezo actuators exhibit a limited range of displacement. One of the most promising solutions to overcome this limitation is to utilize a monolithic type mechanism known as the compliant mechanism. This family of mechanisms could be designed to have an amplification ratio and desired rise time on their output displacement.

Compliant mechanisms, with their zero-backlash and almost infinite resolution, rather simple design structure, have become so popular in the abundance of applications. In recent years, a set of piezo stack actuators and compliant mechanisms have been frequently utilized in researches such as micro and nanopositioning [2, 3], energy harvesting [4], human-machine interaction [5], servo tools precision machining [6], optical devices [7] and so on.

However, compliant mechanisms, with all advantages, are commonly tricky to analyze mathematically. Commercial FEM simulation software is often slow and costly in terms of calculation. For many intentions like performance optimization and control system design, it is necessary to have a fast and relatively accurate analytical solution for the model [8].

Some researchers have proposed several analytical solutions for compliant mechanisms. Ning et al. have established a parametric solution by assimilating the flexible portions as fixed-end flex-tensional beams and solving it by the theory of elasticity [9]. The more basic method of simplification is the pseudo-rigid-body model, which was proposed by Salmon [10] and utilized in many other studies [11, 12].

In other works, Lobontiu et al. [13], presented analytical solutions for corner-filleted and conic-section flexure hinges using Castigliano's second theorem. In addition, a multi-body dynamics model proposed by Ryu has been used to analyze other compliant mechanisms [14, 15].

Recently, a method based on a dynamic stiffness matrix and the D'Alembert principle has been developed by Ling [16-19], which is valid for small deformations. This method has been tested and validated by several compliant mechanisms. This method divides the mechanism into a number of flexible elements, and by achieving the dynamic stiffness matrix of all elements, the global matrix of dynamic stiffness is reachable. Despite the compatibility of this method, in the case of a mechanism with a complex structure, it is tricky to carry out a correct division, considering that the final solution highly depends on the element characteristics.

Besides dynamic and static modeling of the mechanism,

*Corresponding author's email: Ghafarirad@aut.ac.ir

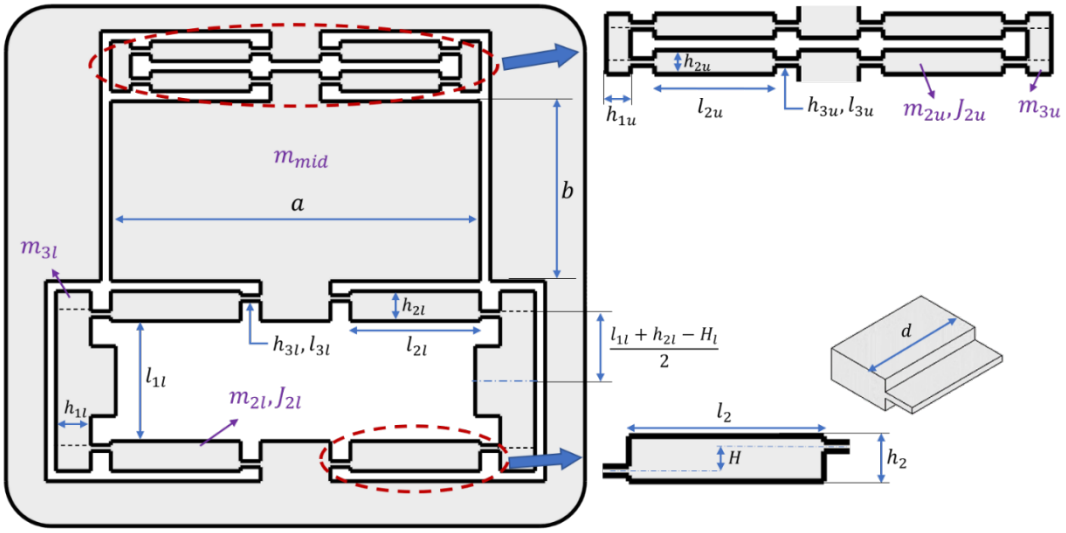


**Fig. 1. Mechanism structure: The parameters h, H, and d represent the length of the segments. m and J denote the mass and moment of inertia of the rigid body segments, respectively. The indices l, u indicate whether the corresponding parameter refers to the upper part or lower part of the mechanism, respectively.**

it is also essential to consider the nonlinear behavior of the piezoelectric, which refers to the hysteresis effect. Various models have been proposed to accurately represent the hysteresis behavior of a system, such as the Preisach [20, 21], Krasnosel'skii–Pokrovskii [22], Prandtl–Ishlinskii [23], Duhem [24] and Bouc–Wen [25] models. Out of these models, the Prandtl–Ishlinskii model which is a subset of the Preisach model is more straightforward, as it overcomes the limitations of the Preisach model [26].

This research introduces a novel compliant amplifying mechanism designed to address a critical limitation of conventional designs, such as bridge or rhombic-type mechanisms: their inherently low out-of-plane stiffness. The proposed mechanism, fully supported from both ends, offers a marked improvement in out-of-plane stiffness while maintaining high amplification performance. The dual-ended support structure of the proposed design not only enhances its performance but also introduces challenges in dynamic and kinetostatic analysis, which are addressed in this study. To evaluate its behavior, three methodologies were employed: analytical modeling, finite element method (FEM), and experimental validation. The static and dynamic analyses were initially conducted using analytical methods to establish a theoretical understanding. To account for nonlinearities, such as the hysteresis inherent to the piezoelectric stack actuator, the Prandtl–Ishlinskii model was utilized. Concurrently, finite element analysis using ANSYS software was conducted to validate and extend the analytical predictions. Finally, a physical prototype was fabricated, and experimental testing confirmed the results obtained from the previous methods.

## 2- Mechanism Configuration

The mechanism structure consists of two bridge-type parts that meet in the middle as shown in Fig. 1.

The first part, which is a conventional bridge-type mechanism supported from the bottom, serves as the component responsible for displacement amplification. The bridge-type mechanism is one of the most common compliant structures which is widely utilized in a variety of applications. This mechanism has been designed with a different type of flexible hinges such as circular, corner-filleted, elliptic, and hyperbolic profiles; In this study, the leaf-spring flexure hinge has been used. The output port of this bridge-type mechanism is connected to a comparatively large, rigid portion that functions as a mounting platform for practical applications. This portion is also connected to a second bridge mechanism, which does not contribute to displacement amplification but fulfills the purpose of supporting the other end of the structure. The second part also provides sufficient flexibility for the initial mechanism to execute its primary function.

Table 1 lists the geometric parameters required for modeling the mechanism.

To demonstrate the advantage of the proposed structure, finite element simulations were conducted to compare its out-of-plane stiffness with a conventional bridge-type mechanism. A slab was attached to both mechanisms, and the tilt caused by the slab's weight was analyzed. As shown in Fig. 2, the proposed mechanism exhibited a tilt of 0.0027 rad, significantly lower than the 0.023 rad observed in the conventional design, highlighting its superior out-of-plane stiffness for high-precision applications.

**Table 1. Main geometrical properties of the mechanism**

| Parameter | Value[mm] | Parameter | Value[mm] | Parameter | Value[mm] | Parameter | Value[mm] |
|---|---|---|---|---|---|---|---|
| $h_{1l}$ | 3.5 | $h_{3l}$ | 0.6 | $h_{1u}$ | 2 | $h_{3u}$ | 0.6 |
| $l_{1l}$ | 12 | $l_{3l}$ | 2 | $l_{1u}$ | 1 | $l_{3u}$ | 2 |
| $h_{2l}$ | 3 | $H_l$ | 1.6 | $h_{2u}$ | 2 | $H_u$ | 0 |
| $l_{2l}$ | 13 | $d$ | 15.4 | $l_{2u}$ | 10 | | |

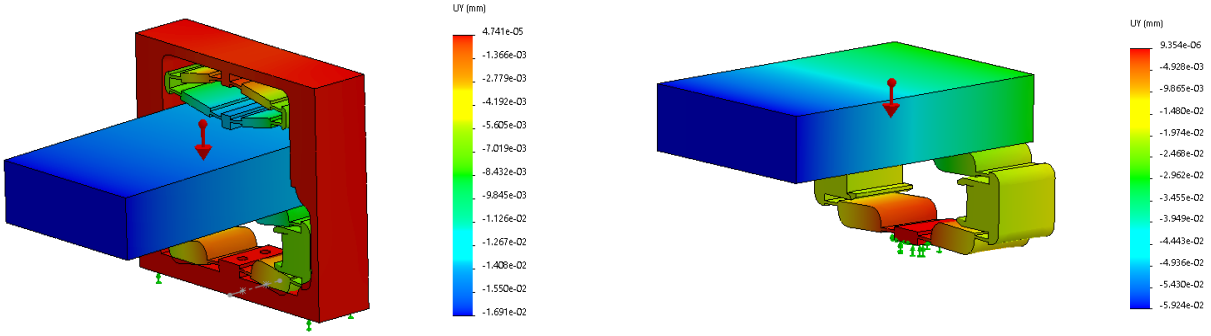


(a) (b)

**Fig. 2. Simulation of (a) proposed and (b) bridge type mechanism under slab weight**

## 3- Kinetostatic and Dynamic Behavior Modeling

In this section, an analytical method is presented to characterize the kinetostatics and dynamics of the compliant mechanism described in section 2. Subsequently, the steps for dynamic and kinetostatic analyses of a lumped compliant mechanism will be explained in the following sections.

### 3- 1- Derivation of Extended Dynamic Stiffness Matrix

The dynamic stiffness matrix characterizes the relation between nodal force and nodal displacement, taking into account the influence of frequency. It can be expressed as Eq. (1)[27].

$$\mathbf{f}^e(\omega) = \mathbf{D}^e(\omega).\mathbf{x}^e(\omega) \tag{1}$$

where ω represents the dynamic frequency (with the unit rad/s), superscript *e* denotes a flexible hinge/beam element. $\mathbf{f}^e(\omega)$ is the vector of applied forces and moments to the nodes of the flexible hinge and $\mathbf{x}^e(\omega)$ is the corresponding displacement vector. $\mathbf{D}^e(\omega)$ denotes the dynamic stiffness matrix.

Eq. (1) can be written in the form of a set of scalar variables as:

$$\begin{bmatrix} N_j^e \\ V_j^e \\ M_j^e \\ N_k^e \\ V_k^e \\ M_k^e \end{bmatrix} = \begin{bmatrix} d_1^e & 0 & 0 & d_5^e & 0 & 0 \\ 0 & d_2^e & -d_3^e & 0 & d_6^e & 0 \\ 0 & -d_3^e & d_4^e & 0 & -d_7^e & d_8^e \\ d_5^e & 0 & 0 & d_1^e & 0 & 0 \\ 0 & d_6^e & -d_7^e & 0 & d_2^e & d_3^e \\ 0 & d_7^e & d_8^e & 0 & d_3^e & d_4^e \end{bmatrix} \begin{bmatrix} u_j^e \\ v_j^e \\ \phi_j^e \\ u_k^e \\ v_k^e \\ \phi_k^e \end{bmatrix} \tag{2}$$

As shown in Fig. 3, the flexible hinge has two nodes *j, k* with 3 degrees of freedom for each node. $u_j^e, v_j^e$ are axial displacements and $N_j^e, N_k^e$ are axial forces; $v_j^e, v_k^e$ are transverse deflections and $V_j^e, V_k^e$ are transverse forces; $\phi_j^e$, $\phi_k^e$ denote rotations and $M_j^e$, $M_k^e$ are moments. $d_i\,(i = 1,2, \ldots, 8)$ are coefficients of the dynamic stiffness matrix $\mathbf{D}^e(\omega)$. For a typical flexible hinge, *j* node corresponds to the node with a smaller number, while the *k* node corresponds to the one with the larger number. This convention is consistently followed in this paper.

For the calculation of these coefficients, it is necessary to

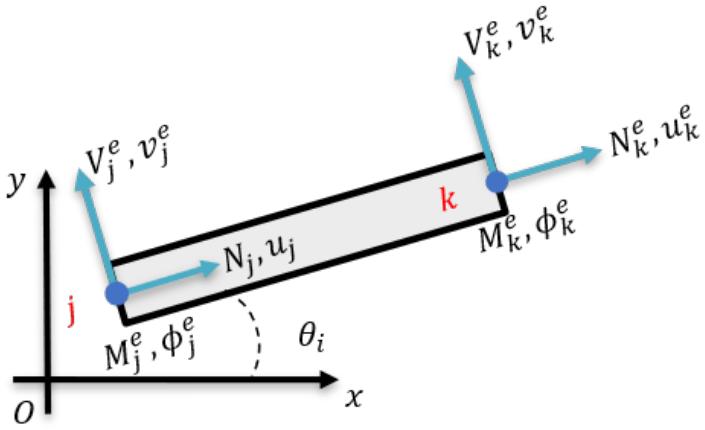


**Fig. 3. A leaf spring flexible hinge: a flexible hinge with label e has 2 nodes with 3 degrees of freedom per node**

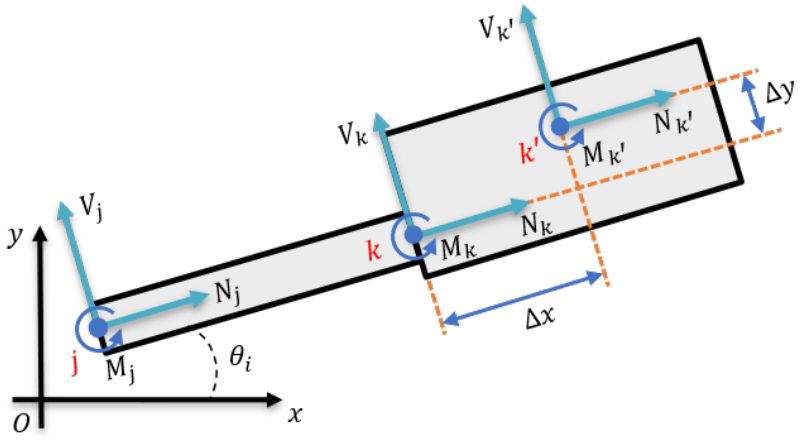


**Fig. 4. Shifting k end node of the flexible hinge to the center of mass of the rigid body**

take a closer look at the definition of the dynamic stiffness matrix. It is well documented in the literature that $\mathbf{D}^e(\omega)$ can be written in the form of Eq. (3)[27].

$$\mathbf{D}^e(\omega) = \mathbf{K}_0 - \omega^2\mathbf{M}_1 - \omega^4\mathbf{M}_2 - \omega^6\mathbf{M}_3 - \cdots \tag{3}$$

where $\mathbf{K}_0$, $\mathbf{M}_1$, $\mathbf{M}_2$ and $\mathbf{M}_3$ are the static stiffness and the first three-order mass matrices of flexible hinges/beams, whose values can be found in reference [27],[28]. In the case of lumped compliant mechanisms with flexible hinges, it is necessary to use the extended dynamic stiffness matrix. Consider a flexible hinge connected from its -end node to a rigid body as shown in Fig. 4.

The purpose is to shift the *k*-end node to the body mass center of the rigid body, which is possible by considering the effect of rigid body motion. This process is exactly shifting the nodal displacement and nodal force at node k to node *k'*. For shifting the displacements from the node *k* to the node *k'*, the relative velocity Eq. (4) is applied for two points *k*, *k'* on a rigid body as:

$$\mathbf{V}_{k'} = \mathbf{V}_{k'} + \boldsymbol{\Omega} \times \mathbf{r}_{k/k'} \tag{4}$$

$$\text{In Eq. (4)}, \mathbf{V}_{k'} = \begin{bmatrix} \frac{du_{k'}}{dt} & \frac{dv_{k'}}{dt} & 0 \end{bmatrix}^{\mathrm{T}} \text{ and } \mathbf{V}_k = \begin{bmatrix} \frac{du_k}{dt} & \frac{dv_k}{dt} & 0 \end{bmatrix}^{\mathrm{T}}$$

are the velocity of nodes *k'* and *k*. $\Omega = \begin{bmatrix} 0 & 0 & -\frac{d\phi_k}{dt} \end{bmatrix}^{\mathrm{T}}$ is the angular velocity of the rigid body connected to the -node of

**Table 2. values of and in terms of geometrical parameters of the mechanism**

| Parameter | Value | Parameter | Value | Parameter | Value |
|---|---|---|---|---|---|
| ($\Delta x_1$, $\Delta y_1$) | (0,0) | ($\Delta x_9$, $\Delta y_7$) | ($l_{2,l}$/ 2, $H_l$/2) | ($\Delta x_{17}$, $\Delta y_{11}$) | ($l_{2,u}$/ 2, 0) |
| ($\Delta x_2$, $\Delta y_2$) | ($l_{2,l}$/ 2, -$H_l$/2) | ($\Delta x_{10}$, $\Delta y_{10}$) | (0,0) | ($\Delta x_{18}$, $\Delta y_{11}$) | ($l_{2,u}$/ 2, 0) |
| ($\Delta x_3$, $\Delta y_3$) | ($l_{2,l}$/ 2, -$H_l$/2) | ($\Delta x_{11}$, $\Delta y_{11}$) | ($l_{2,l}$/ 2, -$H_l$/2) | ($\Delta x_{19}$, $\Delta y_{11}$) | ($l_{2,u}$/ 2, 0) |
| ($\Delta x_4$, $\Delta y_4$) | (0,0) | ($\Delta x_{12}$, $\Delta y_{12}$) | ($l_{2,l}$/ 2, -$H_l$/2) | ($\Delta x_{20}$, $\Delta y_{20}$) | ($l_{2,u}$/ 2, 0) |
| ($\Delta x_5$, $\Delta y_5$) | ($l_{2,l}$/ 2, $H_l$/2) | ($\Delta x_{13}$, $\Delta y_{13}$) | ($l_{2,u}$/ 2, 0) | ($\Delta x_{21}$, $\Delta y_{21}$) | ($l_{2,u}$/ 2, 0) |
| ($\Delta x_6$, $\Delta y_6$) | ($l_{2,l}$/ 2, $H_l$/2) | ($\Delta x_{14}$, $\Delta y_{14}$) | ($l_{2,u}$/ 2, 0) | ($\Delta x_{22}$, $\Delta y_{22}$) | ($l_{2,u}$/ 2, 0) |
| ($\Delta x_7$, $\Delta y_7$) | (0,0) | ($\Delta x_{15}$, $\Delta y_{15}$) | ($l_{2,u}$/ 2, 0) | | |
| ($\Delta x_8$, $\Delta y_8$) | ($l_{2,l}$/ 2, $H_l$/2) | ($\Delta x_{16}$, $\Delta y_{16}$) | ($l_{2,u}$/ 2, 0) | | |

the flexible hinge and $\mathbf{r}_{k'/k} = [\Delta x_i \quad \Delta y_i \quad 0]^{\mathrm{T}}$ is the position of node *k'* relative to the node *k*. Note that $\phi_{k'} = \phi_k$ because the nodes *k* and *k'* are on the same rigid body. By substituting the values for $V_k, V_{k'}, \Omega, r_{k'/k}$ into Eq. (4):

$$\begin{cases} u_{k'} = u_k - \phi_k \Delta y_i \\ v_{k'} = v_k + \phi_k \Delta x_i \\ \phi_{k'} = \phi_k \end{cases} \tag{5}$$

Next, the forces and moments can be shifted from node *k* to node *k'* by using the force equilibrium equations. This results in:

$$\begin{cases} N_{k'} = N_k \\ V_{k'} = V_k \\ M_{k'} = N_k \Delta y_i - V_k \Delta x_i + M_k \end{cases} \tag{6}$$

Using Eq. (5) and Eq. (6), Eqs. (7),(8) can be written as

$$\mathbf{x}^e(\omega) = \begin{bmatrix} u_j \\ v_j \\ \phi_j \\ u_k \\ v_k \\ \phi_k \end{bmatrix} = \begin{bmatrix} 1 & 0 & 0 & 0 & 0 & 0 \\ 0 & 1 & 0 & 0 & 0 & 0 \\ 0 & 0 & 1 & 0 & 0 & 0 \\ 0 & 0 & 0 & 1 & 0 & \Delta y_i \\ 0 & 0 & 0 & 0 & 1 & -\Delta x_i \\ 0 & 0 & 0 & 0 & 0 & 1 \end{bmatrix} \begin{bmatrix} u_j^e \\ v_j^e \\ \phi_j^e \\ u_{k'}^e \\ v_{k'}^e \\ \phi_{k'}^e \end{bmatrix} = \mathbf{T}\boldsymbol{\chi}^e(\omega) \tag{7}$$

$$\mathbf{F}^e(\omega) = \begin{bmatrix} N_j^e \\ V_j^e \\ M_j^e \\ N_{k'}^e \\ V_{k'}^e \\ M_{k'}^e \end{bmatrix} = \begin{bmatrix} 1 & 0 & 0 & 0 & 0 & 0 \\ 0 & 1 & 0 & 0 & 0 & 0 \\ 0 & 0 & 1 & 0 & 0 & 0 \\ 0 & 0 & 0 & 1 & 0 & \Delta y_i \\ 0 & 0 & 0 & 0 & 1 & -\Delta x_i \\ 0 & 0 & 0 & 0 & 0 & 1 \end{bmatrix} \begin{bmatrix} u_j^e \\ v_j^e \\ \phi_j^e \\ u_k^e \\ v_k^e \\ \phi_k^e \end{bmatrix} = \mathbf{T}^{\mathrm{T}}\mathbf{f}^e(\omega) \tag{8}$$

It is worth noting that for the calculation of matrix **T,** the values for $\Delta x_i, \Delta y_i$ are needed. These values are represented in Table 2 for the proposed compliant mechanism.

Using Eqs. (1),(7),(8) yields:

$$\mathbf{F}^e(\omega) = \mathbf{T}^{\mathrm{T}}\mathbf{f}^e(\omega) = \mathbf{T}^{\mathrm{T}}\mathbf{D}^e(\omega)\mathbf{x}^e(\omega) = (\mathbf{T}^{\mathrm{T}}\mathbf{D}^e(\omega)\mathbf{T})\boldsymbol{\chi}^e(\omega) = \mathbf{K}^e(\omega)\boldsymbol{\chi}^e(\omega) \tag{9}$$

In Eq. (9), $\mathbf{F}^e(\omega) = [N_j, V_j, M_j, N_{k'}, V_{k'}, M_{k'}]^{\mathrm{T}}$ and $\chi^e(\omega) = [u_j, v_j, \phi_j, u_{k'}, v_{k'}, \phi_{k'}]^{\mathrm{T}}$. The matrix $\mathbf{K}^e(\omega)$ is called the extended dynamic stiffness matrix and it relates the frequency-dependent relationship between the forces ( $\mathbf{F}^e(\omega)$ )and displacements ( $\chi^e(\omega)$ )at nodes *j* and *k'*.

### 3- 2- Discretization and Numbering the Mechanism

In this step, the mechanism is discretized into flexure hinges, rigid bodies and lumped mass, as shown in Fig. 5.

The marginal ends of two input ports (nodes 2, 5, 8, 10) and similar regions for the upper part (nodes 12, 14, 16, 18) of the mechanism are considered as lumped mass since they have almost no deformation. From geometry the mass for these parts equals $m_{marginal} = \frac{\rho h_1 d(H + h_2)}{2}$, where $\rho$ denotes

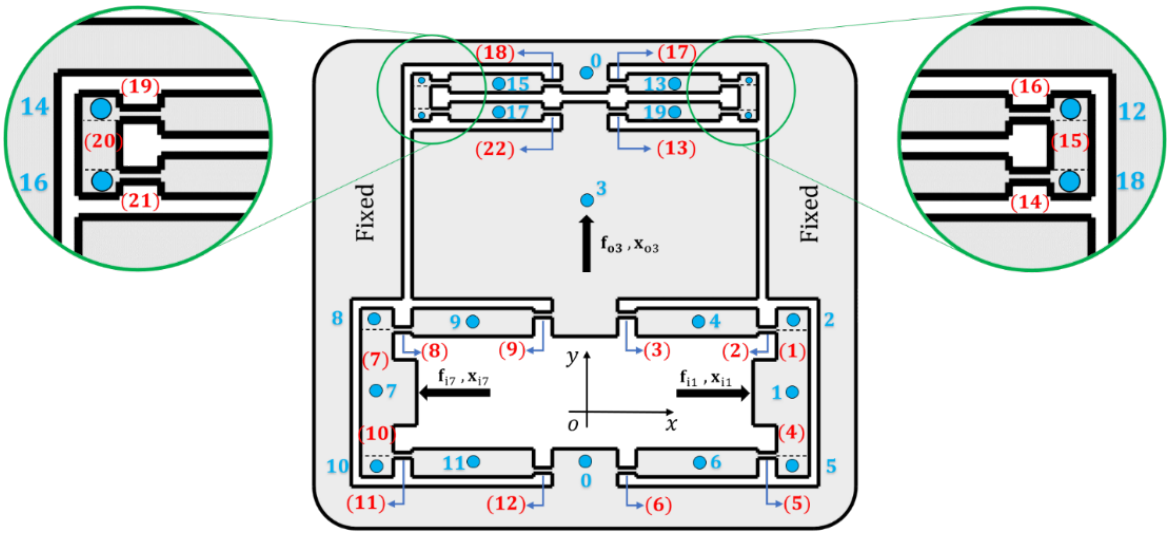


**Fig. 5. Discretization and numbering of nodes and elements of the compliant mechanism: nodes 1 and 7 are the input ports of the mechanism, and node 3 is the output port.**

density and $h_1$, $d$, $H$, $h_2$ are geometrical parameters (shown in Fig. 1). These parameters have different numerical values for the lower and upper parts of the mechanism. As mentioned before in section 3.1, two nodes are considered for each flexible hinge. The node with the larger number is named -node, and the other node is named $j$-node. The flexible hinges are numbered from (1) to (22) and connected with nodes labeled as blue circles. All nodes were numbered from 0 to 19 and the nodes with the number 0 are clamped nodes that specify the boundary conditions of the mechanism. During the numbering, the $k$-end node of flexure hinges/beams connected to a rigid body was shifted to the mass center. This procedure was explained in detail in section 3.1. The effect of the piezoelectric actuator at the input of the mechanism is considered as force $\mathbf{f}_{in}$ or displacement $\mathbf{x}_{in}$. In addition, for calculating the output stiffness of the mechanism, a dummy force $\mathbf{f}_{out}$ is applied on the output port. Vector form of these forces and displacements are as follows:

$$\begin{cases} \mathbf{f}_{in1} = -\mathbf{f}_{in7} = [f_i \quad 0 \quad 0]^{\mathrm{T}} \\ \mathbf{x}_{in1} = -\mathbf{x}_{in7} = [x_i \quad 0 \quad 0]^{\mathrm{T}} \\ \mathbf{f}_{out} = -\mathbf{f}_{out} = [0 \quad f_{out} \quad 0]^{\mathrm{T}} \\ \mathbf{x}_{out} = -\mathbf{x}_{out} = [0 \quad f_{out} \quad 0]^{\mathrm{T}} \end{cases} \tag{10}$$

### 3- 3- Force Equilibrium Equations

In this step, Force equilibrium equations are developed for the compliant mechanism in the frequency domain. Since these equilibrium equations are driven in the reference coordinate system $oxy$, the extended dynamic stiffness matrix for each flexible element must be transferred to this coordinate frame. For the $i^{\text{th}}$ flexible hinge, the rotation matrix is determined according to Eq. (11):

$$\mathbf{R}_i = \begin{bmatrix} \cos\theta_i & \sin\theta_i & 0 & 0 & 0 & 0 \\ -\sin\theta & \cos\theta_i & 0 & 0 & 0 & 0 \\ 0 & 0 & 1 & 0 & 0 & 0 \\ 0 & 0 & 0 & \cos\theta & \sin\theta & 0 \\ 0 & 0 & 0 & -\sin\theta & \cos\theta & 0 \\ 0 & 0 & 0 & 0 & 0 & 1 \end{bmatrix} \tag{11}$$

In Eq. (11), $\theta_i$ is the orientation angle for the $i^{\text{th}}$ flexible hinge. For the proposed mechanism, these values are listed in Table 3.

The extended dynamic stiffness matrix of all flexure hinges in the reference coordinate frame can be denoted as:

$$\mathbf{K}_i(\omega) = \mathbf{R}_i^{\mathrm{T}} \mathbf{K}^e(\omega) \mathbf{R}_i \tag{12}$$

For better formulation, the frequency-dependent relationship between nodal displacement and nodal force of the $i^{\text{th}}$ flexure hinge in the reference frame $oxy$ can be written in matrix form as follows:

**Table 3. Values of θi for each flexure hinge**

| Parameter | Value | Parameter | Value | Parameter | Value | Parameter | Value |
|---|---|---|---|---|---|---|---|
| $\theta_1$ | 90° | $\theta_7$ | 90° | $\theta_{13}$ | 0 | $\theta_{19}$ | 0 |
| $\theta_2$ | 180° | $\theta_8$ | 0 | $\theta_{14}$ | 180° | $\theta_{20}$ | -90° |
| $\theta_3$ | 0 | $\theta_9$ | 180° | $\theta_{15}$ | -90° | $\theta_{21}$ | 0 |
| $\theta_4$ | -90° | $\theta_{10}$ | -90° | $\theta_{16}$ | 180° | $\theta_{22}$ | 180° |
| $\theta_5$ | 180° | $\theta_{11}$ | 0 | $\theta_{17}$ | 0 | | |
| $\theta_6$ | 0 | $\theta_{12}$ | 180 ° | $\theta_{18}$ | 180° | | |

$$\begin{cases} \mathbf{F}_i(\omega)=\begin{bmatrix}\mathbf{F}_{i,j}\\ \mathbf{F}_{i,k}\end{bmatrix}=\begin{bmatrix}\mathbf{k}_{i,1} & \mathbf{k}_{i,2}\\ \mathbf{k}_{i,3} & \mathbf{k}_{i,4}\end{bmatrix}\begin{bmatrix}\mathbf{x}_{i,j}\\ \mathbf{x}_{i,k}\end{bmatrix} \\ \mathbf{F}_{i,j}(\omega)=[N_{i,j} \quad V_{i,j} \quad M_{i,j}]^{\mathrm{T}}, \\ \mathbf{F}_{i,k}(\omega)=[N_{i,k} \quad V_{i,k} \quad M_{i,k}]^{\mathrm{T}} \\ \mathbf{x}_{i,j}=[u_{i,j} \quad v_{i,j} \quad \phi_{i,j}]^{\mathrm{T}}, \\ \mathbf{x}_{i,k}=[u_{i,k} \quad v_{i,k} \quad \phi_{i,k}]^{\mathrm{T}} \end{cases} \tag{13}$$

In Eq. (13), $\mathbf{k}_{i,1}, \mathbf{k}_{i,2}, \mathbf{k}_{i,3}, \mathbf{k}_{i,4}$ are 3×3 submatrices of $\mathbf{K}^e(\omega)$. $\mathbf{F}_{i,j}$, $\mathbf{F}_{i,k}$, $\mathbf{x}_{i,j}$, $\mathbf{x}_{i,k}$ are the nodal forces and nodal displacements of the $i^{\text{th}}$ flexure hinge in *oxy* coordinate system. Consequently, Eq. (14) is applicable to each node of $i^{\text{th}}$ flexure hinge:

$$\begin{cases} \mathbf{F}_{i,j}(\omega)=\mathbf{k}_{i,1}\mathbf{x}_{i,j}+\mathbf{k}_{i,2}\mathbf{x}_{i,k} \\ \mathbf{F}_{i,k}(\omega)=\mathbf{k}_{i,3}\mathbf{x}_{i,j}+\mathbf{k}_{i,4}\mathbf{x}_{i,k} \end{cases} \tag{14}$$

In the analysis of each node, it is essential to consider three distinct types of forces [18]. The first type is the force exerted by the flexure hinges which is connected to, but in the opposite direction. The second is the force caused by the node's own mass if it is a lumped mass or a rigid body. The third type is any external forces acting on the node. Using D'Alembert's principle, the force equilibrium equations can be established in the frequency domain.

$$\begin{cases} \text{Node 1} & \mathbf{f}_{in1}(\omega)=\mathbf{F}_{1,j}+\mathbf{F}_{4,j} \\ \text{Node 2} & \mathbf{0}=\mathbf{F}_{1,k}+\mathbf{F}_{2,j}+\mathbf{M}_2\mathbf{x}_2 \\ \text{Node 3} & \mathbf{0}=\mathbf{F}_{3,j}+\mathbf{F}_{9,j}+\mathbf{F}_{13,j}+\mathbf{F}_{22,j}+\mathbf{M}_3\mathbf{x}_3 \\ \text{Node 4} & \mathbf{0}=\mathbf{F}_{2,k}+\mathbf{F}_{3,k}+\mathbf{M}_4\mathbf{x}_4 \\ \text{Node 5} & \mathbf{0}=\mathbf{F}_{4,k}+\mathbf{F}_{5,j}+\mathbf{M}_5\mathbf{x}_5 \\ \text{Node 6} & \mathbf{0}=\mathbf{F}_{5,k}+\mathbf{F}_{6,k}+\mathbf{M}_6\mathbf{x}_6 \\ \text{Node 7} & \mathbf{f}_{i,2}(\omega)=\mathbf{F}_{7,j}+\mathbf{F}_{10,j} \\ \vdots & \vdots \\ \text{Node 18} & \mathbf{0}=\mathbf{F}_{14,j}+\mathbf{F}_{15,k}+\mathbf{M}_{18}\mathbf{x}_{18} \\ \text{Node 19} & \mathbf{0}=\mathbf{F}_{13,k}+\mathbf{F}_{14,k}+\mathbf{M}_{19}\mathbf{x}_{19} \end{cases} \tag{15}$$

where $\mathbf{f}_{i,1}=[f_{i,1},0,0]^{\mathrm{T}}$ and $\mathbf{f}_{i,2}=[f_{i,2},0,0]^{\mathrm{T}}$.
In addition, the mass matrix $\mathbf{M}_{\mathrm{n}}$ can be expressed as:

$$\mathbf{M}_n(\omega)=\begin{bmatrix}-m\omega^2 & 0 & 0\\ 0 & -m\omega^2 & 0\\ 0 & 0 & -J\omega^2\end{bmatrix} \tag{16}$$

Here, stands for the mass of the $n^{\text{th}}$ node. Mass moment inertia *J* is defined with respect to the mass center and is set to zero for a lumped mass since it is very small and does not contribute to any rotation in the problem.

Using Eq. (14) and Eq. (15), it yields to:

$$\begin{cases} \text{Node 1} & \mathbf{f}_{i,1}(\omega)=(\mathbf{k}_{1,1}+\mathbf{k}_{4,1})\mathbf{x}_1+\mathbf{k}_{1,2}\mathbf{x}_2+\mathbf{k}_{4,2}\mathbf{x}_5 \\ \text{Node 2} & \mathbf{0}=\mathbf{k}_{1,3}\mathbf{x}_1+(\mathbf{k}_{1,4}+\mathbf{k}_{2,1}+\mathbf{M}_2)\mathbf{x}_2+\mathbf{k}_{2,2}\mathbf{x}_4 \\ \text{Node 3} & \mathbf{0}=(\mathbf{k}_{3,1}+\mathbf{k}_{9,1}+\mathbf{k}_{13,1}+\mathbf{k}_{22,1}+\mathbf{M}_3)\mathbf{x}_3+\mathbf{k}_{3,2}\mathbf{x}_4+\mathbf{k}_{9,2}\mathbf{x}_9+\mathbf{k}_{22,2}\mathbf{x}_{17}+\mathbf{k}_{13,2}\mathbf{x}_{19} \\ \text{Node 4} & \mathbf{0}=\mathbf{k}_{2,3}\mathbf{x}_2+\mathbf{k}_{3,3}\mathbf{x}_3+(\mathbf{k}_{2,4}+\mathbf{k}_{3,4}+\mathbf{M}_4)\mathbf{x}_4 \\ \text{Node 5} & \mathbf{0}=\mathbf{k}_{4,3}\mathbf{x}_1+(\mathbf{k}_{4,4}+\mathbf{k}_{5,1}+\mathbf{M}_5)\mathbf{x}_5+\mathbf{k}_{5,2}\mathbf{x}_6 \\ \text{Node 6} & \mathbf{0}=\mathbf{k}_{5,3}\mathbf{x}_5+\mathbf{k}_{6,3}\mathbf{0}+(\mathbf{k}_{5,4}+\mathbf{k}_{6,4}+\mathbf{M}_6)\mathbf{x}_6 \\ \text{Node 7} & \mathbf{f}_{i,2}(\omega)=(\mathbf{k}_{7,1}+\mathbf{k}_{10,1})\mathbf{x}_7+\mathbf{k}_{7,2}\mathbf{x}_8+\mathbf{k}_{10,2}\mathbf{x}_7 \\ \vdots & \vdots \\ \text{Node 18} & \mathbf{0}=\mathbf{k}_{15,3}\mathbf{x}_{12}+(\mathbf{k}_{14,1}+\mathbf{k}_{15,4}+\mathbf{M}_{18})\mathbf{x}_{18}+\mathbf{k}_{14,2}\mathbf{x}_{19} \\ \text{Node 19} & \mathbf{0}=\mathbf{k}_{13,3}\mathbf{x}_3+\mathbf{k}_{14,3}\mathbf{x}_{18}+(\mathbf{k}_{13,4}+\mathbf{k}_{14,4}+\mathbf{M}_{19})\mathbf{x}_{19} \end{cases} \quad (17)$$

To derive the dynamic stiffness model of the displacement amplification mechanism presented, Eq. (17) can be rewritten in matrix form as Eq. (18):

$$\begin{cases} \begin{bmatrix} \mathbf{f}_{i,1} \\ \mathbf{0} \\ \mathbf{f}_{o,3} \\ \mathbf{0} \\ \vdots \\ \mathbf{f}_{i,7} \\ \vdots \\ \mathbf{0} \end{bmatrix} = \mathbf{D}(\omega) \begin{bmatrix} \mathbf{x}_1 \\ \mathbf{x}_2 \\ \mathbf{x}_3 \\ \mathbf{x}_4 \\ \vdots \\ \mathbf{x}_7 \\ \vdots \\ \mathbf{x}_{19} \end{bmatrix} \\ \mathbf{D}(\omega)=\begin{bmatrix} \mathbf{k}_{1,1}+\mathbf{k}_{4,1} & \mathbf{k}_{1,2} & \cdots & \mathbf{0} \\ \mathbf{k}_{1,3} & \mathbf{k}_{1,4}+\mathbf{k}_{2,1}+\mathbf{M}_2 & \cdots & \mathbf{0} \\ \vdots & \vdots & \ddots & \vdots \\ \mathbf{0} & \mathbf{0} & \cdots & \mathbf{k}_{13,4}+\mathbf{k}_{14,4}+\mathbf{M}_{19} \end{bmatrix} \end{cases} \quad (18)$$

in which, $\mathbf{D}(\omega)$ is the dynamic stiffness of the whole compliant mechanism.

### 3- 4- Hysteresis Behavior Modeling

Prandtl-Ishlinskii model is a mathematical approach used to describe and simulate the behavior of hysteresis in systems [23]. Hysteresis refers to the phenomenon where the output of a system depends not only on the current input but also on its history.

The first operator in this model is the backlash operator, as shown in Fig. 6, and is defined by Eq. (19)[29]. This Operator is independent of the hysteresis and often utilized for modeling the backlash between gears.

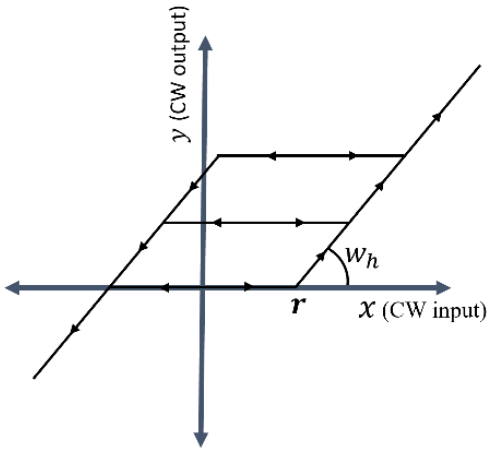


**Fig. 6. Backlash operator with threshold rand weighting value $w_h$**

$$\begin{cases} y(t)=H_r[x,y_0](t)= \\ \max\{x(t)-t,\min\{x(t)+r,y(t-\tau)\}\} \\ y(0)=\max\{x(0)-r, \\ \quad \min\{x(0)+r,y_0\}\} \end{cases} \quad (19)$$

In Eq. (19), $x$ represents the system input, $y$ represents the output response, $r$ represents the input threshold value or the magnitude of the backlash, and $\tau$ represents the sampling period. The initial consistency condition $y_0$ does not necessarily need to be initialized to zero. To create the generalized backlash operator, the backlash operator $H_r$ is multiplied by a weight value $w_h$.

$$y(t)=w_h H_r(x,y_0)(t) \quad (20)$$

The $w_h$ parameter is the weight that could be tuned to the exact backlash model.

A complicated hysteresis nonlinearity can be simulated using a linearly weighted combination of multiple backlash operators, each with unique threshold and weight values.

$$y(t)=\sum_{i=1}^{n} w_h^{\tau^i} H_r^i[x,y_0](t) \quad (21)$$

## 4- Simulation Results

In this section, the kinetostatic and dynamic behavior of the mechanism are studied using the analytical method introduced in section 3. Also, the results from the analytical

solution are compared with those obtained from the finite element method.

### 4- 1- Kinetostatic Behavior

The kinetostatic results for the mechanism can be obtained by solving the linear system of Eq. (18) with the dynamic frequency ω = 0; static properties of the mechanism can be calculated by Eq. (22).

$$R = \frac{x_{3y}}{x_{1x} - x_{7x}}, \qquad K_{in} = \frac{f_{in}}{x_{1x} - x_{7x}}, \quad K_{out} = \frac{f_{out}}{x_{3y}} \tag{22}$$

where $R$ represents the displacement amplification ratio, $K_{in}$ is the input stiffness and $K_{out}$ is the output stiffness of the mechanism.

Also, Finite Element Method (FEM) simulations are conducted using the ANSYS Workbench software package. For modeling, aluminum alloy 7075 is selected, which has a density (ρ) of 2770 kg/m$^3$, Young's modulus ($E$) of 71 GPa, and shear modulus ($G$) of 27 GPa. SOLID186 elements, along with an advanced size function, "capture proximity" were employed to refine the mesh. After verifying the finite element software solutions, a converged mesh of approximately one hundred thousand computing nodes was selected.

In order to determine the output stiffness, various magnitudes of force are applied to the output port of the mechanism. A force-displacement diagram was generated using data from both ANSYS software and analytical methods. A similar process is performed to calculate the mechanism's input stiffness and displacement amplification ratio. Fig. 7 shows these diagrams.

The results of static properties are given in Table 4.

### 4- 2- Dynamic Behavior

This section aims to compute the first natural frequency of the compliant amplifying mechanism. To achieve this, the set of Eq. (18) has been solved for frequencies ranging from 1 to 1000 Hz, with an increase of 1 Hz at each step. The natural frequency is determined by identifying the frequency at which the maximum output amplitude occurs. The frequency response of the mechanism obtained from both analytical and finite element methods is presented in Fig. 8.

Another approach for finding the natural frequencies of the mechanism is to use the roots of the determinant of the matrix **D**(ω). The determinant of the dynamic stiffness matrix is calculated using frequencies ranging from 1 to 1000 Hz, with an increase of 1Hz at each step. Fig. 9 shows the diagram of the determinant of the **D**(ω) matrix as well as the mode shapes of the mechanism, which are extracted from the finite element software package.

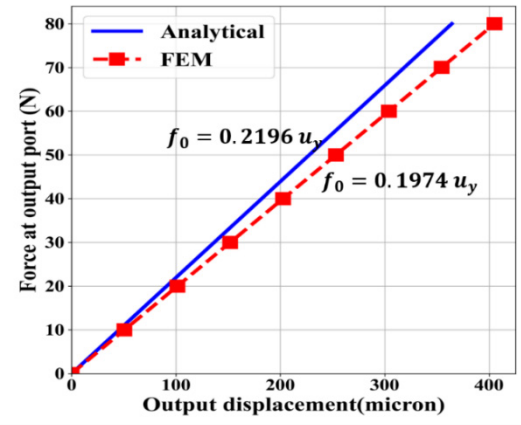


(a)

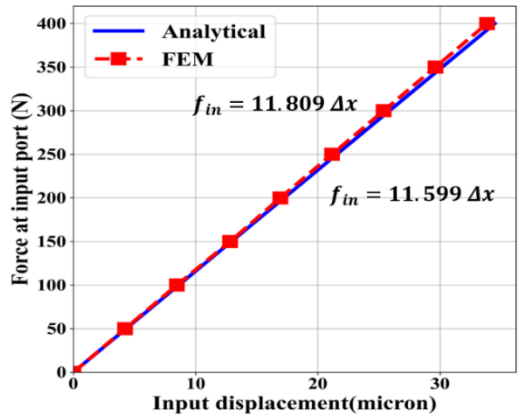


(b)

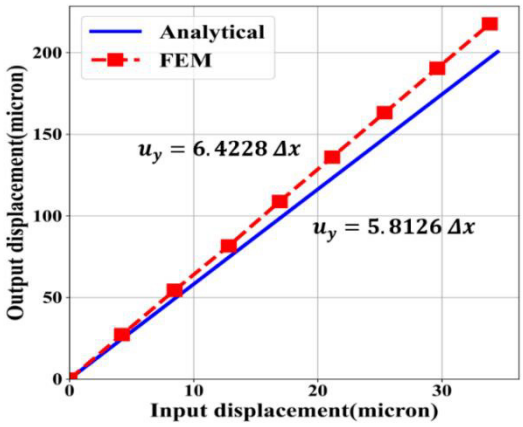


(c)

**Fig. 7. Static properties of the mechanism: (a) output stiffness, (b) input stiffness, (c) amplification ratio. The output displacement corresponds to the displacement of node 7 (the output port of the mechanism), while the input displacement is the difference between the displacements of nodes 1 and 7 (the input ports of the mechanism).**

**Table 4. Static properties of the mechanism: output stiffness (Kout), input stiffness (Kin), and amplification ratio (R) obtained through analytical, FEM**

| Solution method | $K_{out}$ | $K_{in}$ | $R$ |
|---|---|---|---|
| Analytical | 0.2196 | 11.599 | 5.8126 |
| FEM | 0.1974 | 11.809 | 6.4228 |
| Error | 11.25% | 1.78% | 9.50% |

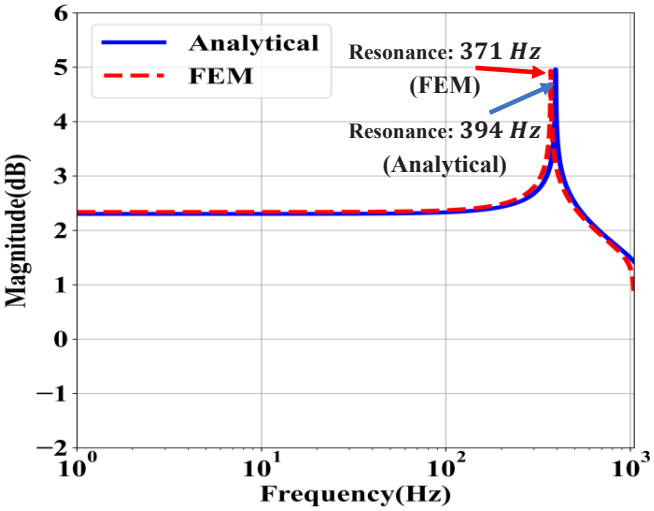


**Fig. 8. Frequency response of the mechanism: displacement of the output port of the mechanism in the frequency range of 1 to 1000 Hz**

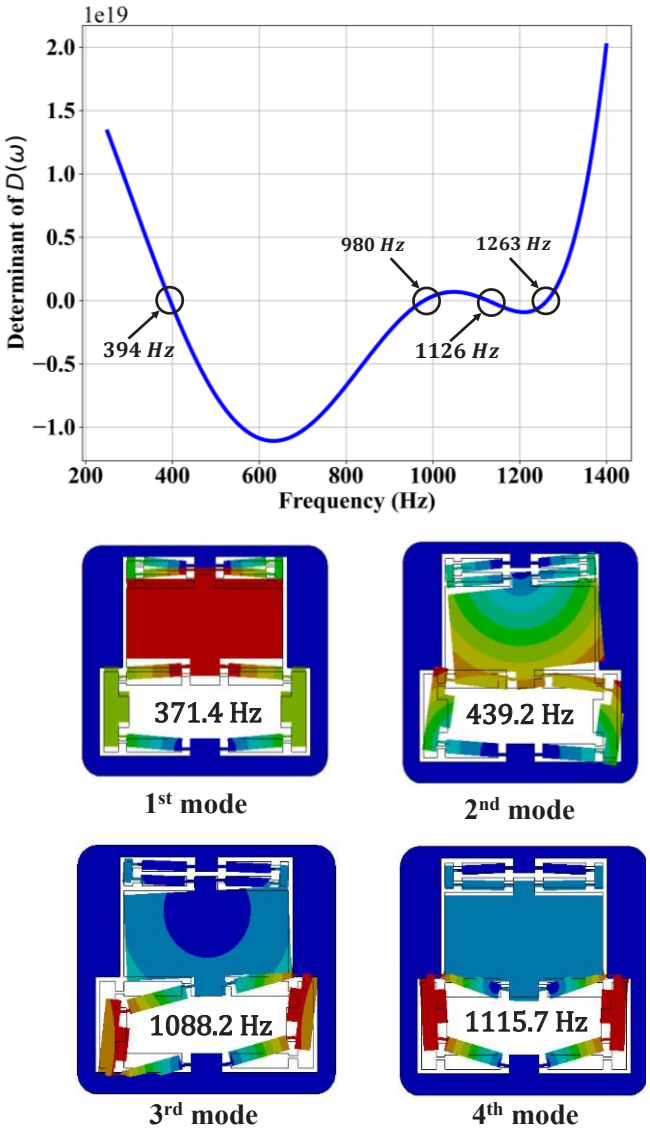


**Fig. 9. Searching the roots of the determinant of the dynamic stiffness matrix D(ω) and the finite element results of mode shapes**

## 5- Experimental Testing

An experimental setup has been arranged to validate the developed methodology. As illustrated in Fig. 10, the components of this setup comprise a prototype of a compliant mechanism that is crafted from aluminum (7075 T6). The compliant mechanism was fabricated using a wire-electrode cutting technique. The complete amplifier has dimensions of 52 mm × 58 mm × 15.4 mm and was securely fastened to a table using screws during dynamic measurements to minimize the influence of ground vibrations. The piezoelectric and power amplifiers utilized in this experiment are SA050536 and PDu150, both from PiezoDrive Co. The piezoelectric stacks were assembled into the displacement amplification mechanism using an interference fit with a tolerance of approximately 2 μm. The output displacement of the compliant mechanism was measured using a precision optical sensor (MicroEpsilon-ILD2300). A 3D-printed solid block was fastened to the middle part of the mechanism (which is the output port) to facilitate accurate displacement readings. The data of the optical sensor is recorded by a data acquisition card (NI 6052E).

### 5- 1- Kinetostatics

The static properties of the mechanism include the amplification ratio and stiffness. The amplification ratio is determined by measuring the displacement of the input and output ports of the mechanism and calculating the ratio of these displacements. It is important to note that the input port

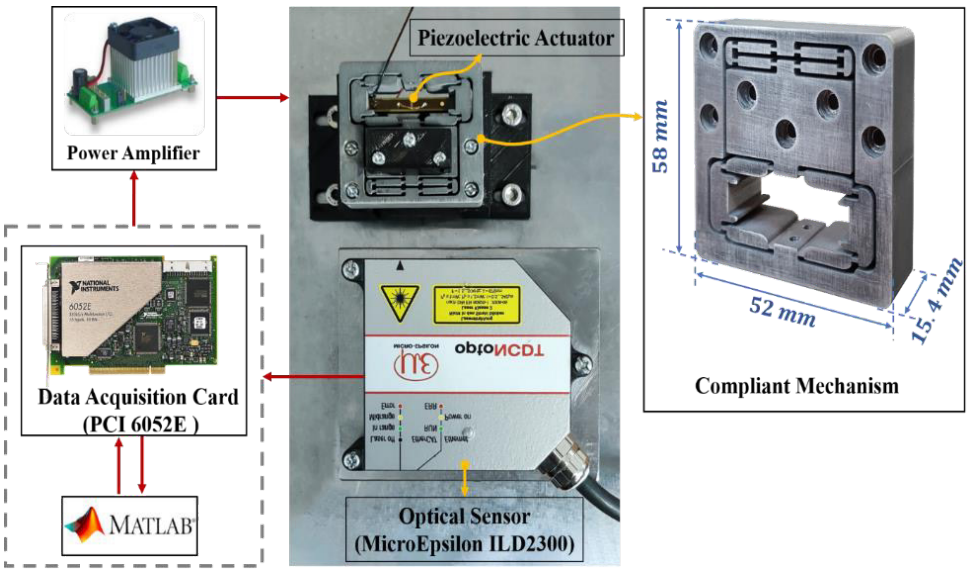


**Fig. 10. Experimental setup block diagram**

displacement is only recorded from one port and multiplied by a factor of 2, as the input displacement is identical for both input ports. As depicted in Fig. 11 the input signal in this experiment is a sine wave with a period of 5 seconds.

The stiffness of the output port of the mechanism can be determined through a precise experiment. By attaching varying weights to the output port, as shown in Fig. 12, and recording the displacement with an optical sensor (CD22-Optex), the ratio of the applied force to the generated displacement can be calculated to reveal the stiffness of the output port.

It is essential to mention that neither analytical nor FEM simulations involved the piezoelectric in the compliant mechanism. Thus, this experiment followed the same methodology.

### 5- 2- Dynamic Behavior

To test the dynamic response of the mechanism, a chirp signal was applied to the actuator. This signal had an excitation frequency that increased from 0.1 to 500 Hz over a duration of 200 seconds, with a constant amplitude of 5V. An FFT was performed on the signal in Fig. 13 to identify the natural frequencies in the frequency domain.

### 5- 3- Hysteresis Identification

The identification process was conducted using experimental data to predict the hysteretic behavior of the actuator. It should be noted that the modeling was specifically focused on the nonlinear hysteresis behavior that arises inherently at low frequencies, where dynamic effects such as damping, inertia, and resonance are negligible [26, 29].

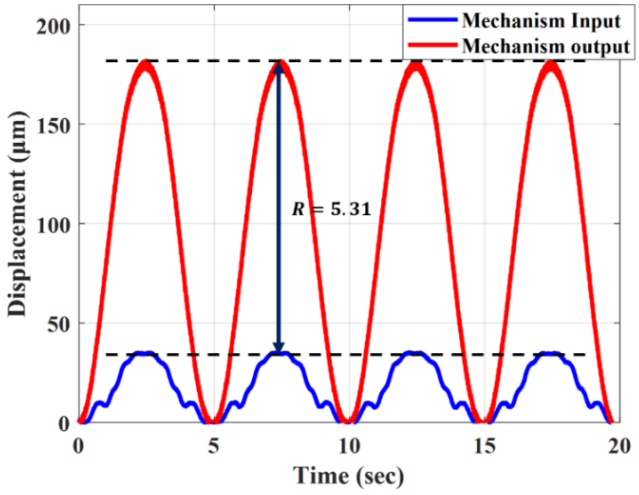


**Fig. 11. Amplification ratio of the mechanism**

To ensure accuracy and reliability, the experiments were deliberately performed at low frequencies. By adopting this approach, interference from the dynamic characteristics of the system, particularly damping, was minimized, thereby allowing the intrinsic hysteretic behavior of the system to be isolated.

The input signal is a quasi-static triangular wave with a period of , , and second as is evident in Fig. 14. The identified loop has been demonstrated alongside the actual loop for

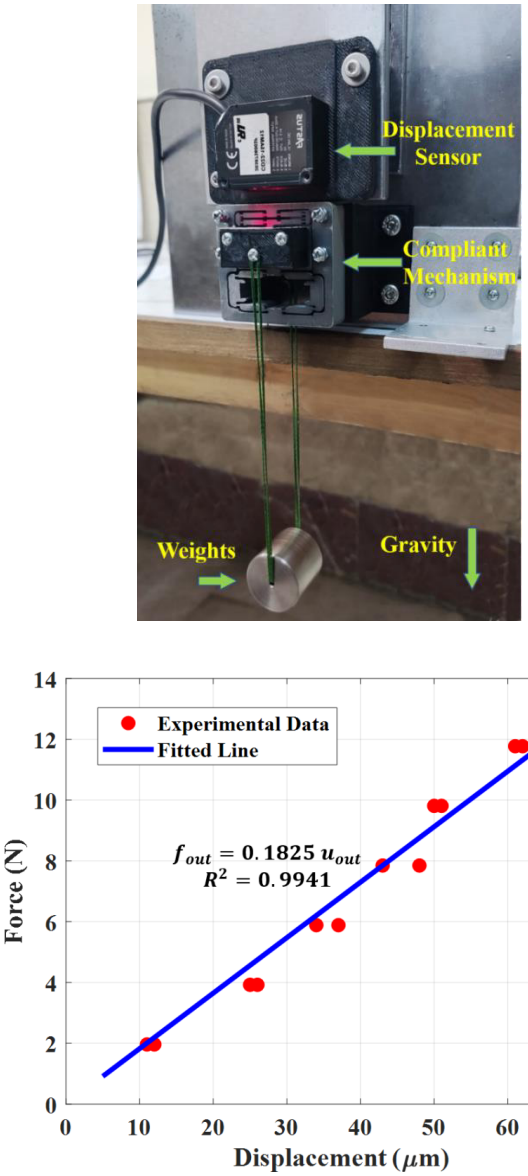


**Fig. 12. Upper section: The experimental setup for determining the output stiffness (Kout) of the mechanism. Lower section: Force vs. displacement diagram at the output port.**

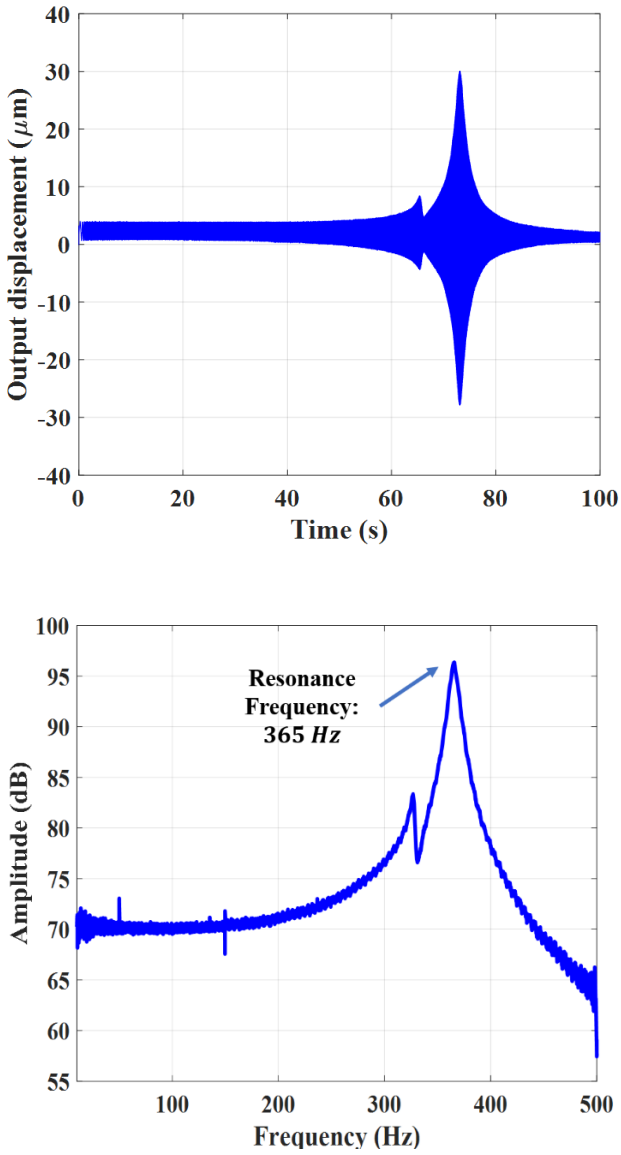


**Fig. 13. Response of the mechanism to chirp signal in time and frequency domain**

comparison in Fig. 15.

Table 5 shows the identification error for the hysteresis behavior.

## 6- Discussion

In this section, all obtained results have been compared and discussed.

### 6- 1- Static characteristics

The static properties of the mechanism are listed in Table 6. The analytical method in amplification ratio has about 9.5% deviation from the FEM method, with a similar 9.5% error compared to the experimental results. The output stiffness of the mechanism obtained by the analytical method has 11.25% error in comparison with the FEM software result. The output stiffness was also investigated experimentally and its analogy with the analytical method showed about 20.33% difference. The input stiffness of the mechanism compared to FEM results showed about 1.78% of error.

One reason for the difference between the analytical/FEM results and experimental results is that the prototype's flexible hinges have fillets, which are challenging to fabricate in the idealized leaf-spring model used in simulations. However, this discrepancy is not entirely detrimental, as filleted hinges reduce stress concentration, whereas leaf-spring hinges may induce high stress concentrations. Additionally,

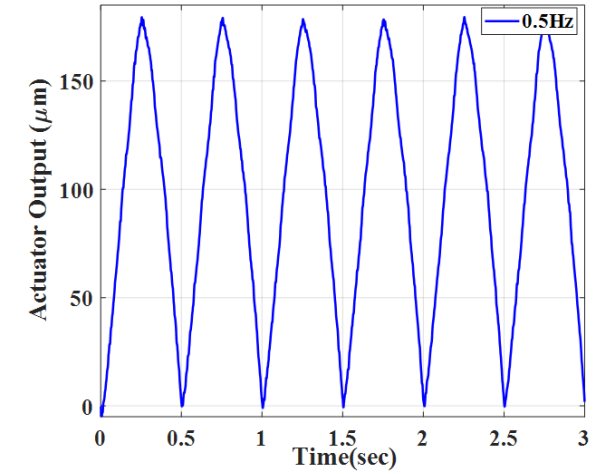


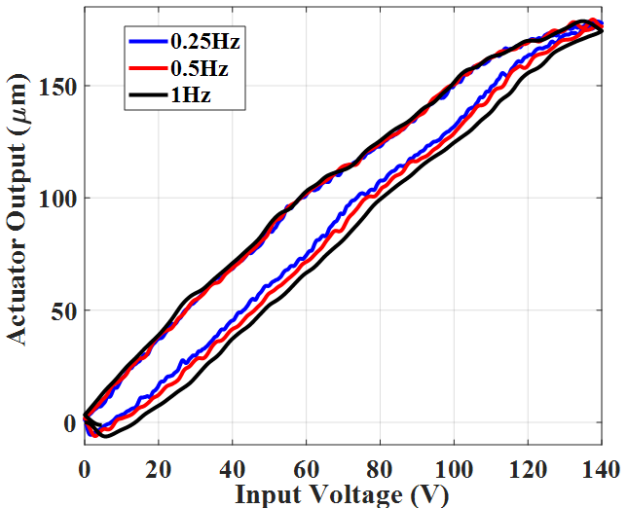


**Fig. 14. Experimental results of the triangular quasi-static input and open-loop hysteresis**

**Table 5. RMSE and NRMSE for each frequency**

| Frequency (Hz) | RMSE (μm) | NRMSE (%) | $R^2$ |
|---|---|---|---|
| 0.25 | 1 | 1.7 | 0.989 |
| 0.5 | 1.46 | 1.31 | 0.993 |
| 1 | 1.90 | 1.74 | 0.991 |

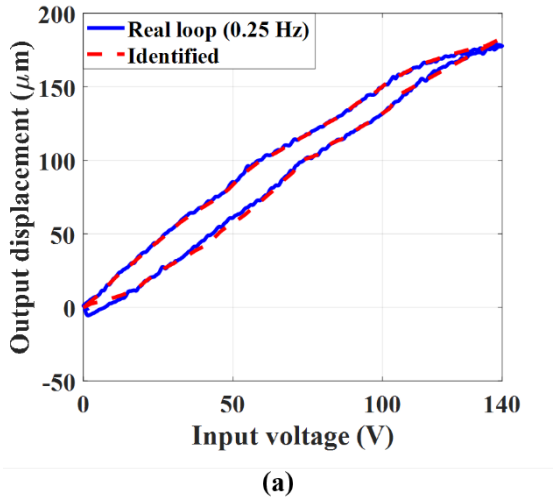


(a)

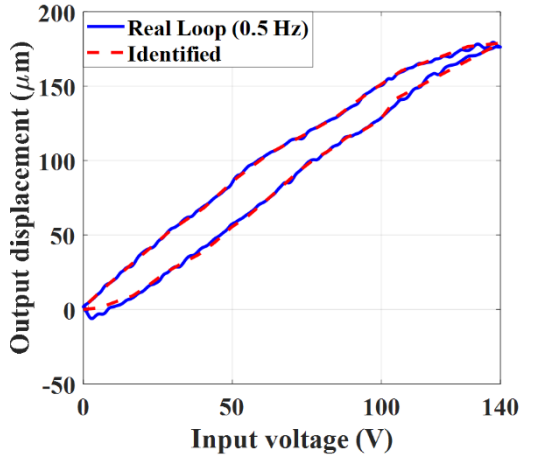


(b)

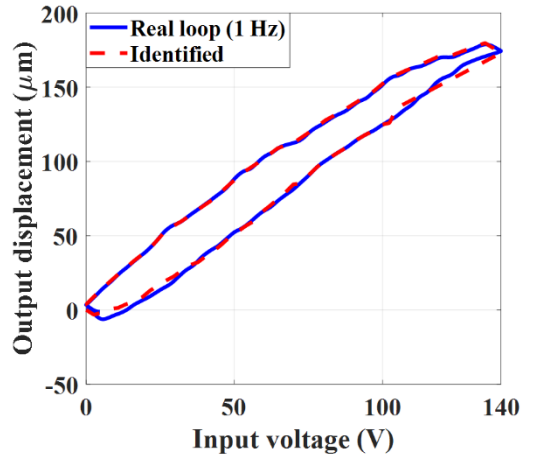


(c)

**Fig. 15. Real and identified hysteresis loop with Prandtl–Ishlinskii model in (a) 0.25 Hz (b) 0.5 Hz (c) 1 Hz**

**Table 6. Static properties of the mechanism: output stiffness (Kout), input stiffness (Kin), and amplification ratio (R) obtained through analytical, FEM, and experimental methods**

| Static properties | Analytical | FEM | Experimental |
|---|---|---|---|
| $R$ | 5.8126 | 6.4228 | 5.31 |
| $K_{out}$ [N/μm] | 0.2196 | 0.1974 | 0.1825 |
| $K_{out}$ [N/μm] | 11.599 | 11.809 | - |

**Table 7. Results obtained for frequencies of the mode shapes of the mechanism**

| Vibration mode | Analytical [Hz] | FEM [Hz] | Experimental [Hz] |
|---|---|---|---|
| Mode 1 | 394 | 371 | 365 |
| Mode 2 | 980 | 439 | |
| Mode 3 | 1126 | 1088 | |
| Mode 4 | 1263 | 1115 | |

it was inevitable to use a piezoelectric actuator to drive the mechanism in experiments due to its precision and high-frequency capabilities. The actuator has its own stiffness and nonlinear hysteresis behavior, which impacts the results.

The overall performance of the analytical method in static properties has adequate accuracy in comparison with commercial FEM software (ANSYS) and especially with experimental results.

### 6- 2- Dynamic characteristics

Obtained results from the investigation on resonant modes of the system in analytical, FEM and experimental methods have been demonstrated in Table 7.

In Table 7, it is shown that the first natural frequency mode has a deviation of approximately 6.2% and 7.9% from the FEM and experimental results respectively. The first frequency mode is the most important among others since it is a representation of system response time and the safe working frequency spectrum of the system. In the analytical method, the second natural frequency of the system was obtained via a large error. This may be due to the fact that the second mode shape involves large rotations for the rigid middle part of the mechanism. In the analytical model, this middle part is treated as a lumped mass and does not undergo any rotational motion. The analytical method exhibits an error of approximately 3.5% and 13% in the third and fourth resonant modes of the system, respectively. It is worth noting that in the third mode also the rigid middle part rotates, but the magnitude of rotation is small enough so that this mode can be predicted via an acceptable error by the analytical method. Considering the modeling method and its inherent limitations, the overall accuracy of the method in predicting the dynamic properties of the system is acceptable.

### 6- 3- Hysteresis behavior

Based on the root mean square error (RMSE) and normalized root mean squared error (NRMSE) and $R^2$ stated in Table 5 for the hysteresis model's accuracy, it can be inferred that the error in position prediction across all three frequencies is confined within a limited range, and the proposed model effectively captures the system's hysteresis behavior with high accuracy.

In this study, the piezoelectric actuator's hysteresis behavior was modeled separately, as the focus was on modeling the compliant mechanism. However, Future work could integrate coupled modeling approaches to further improve the overall system representation.

## 7- Conclusion

Compliant mechanisms with exceptional advantages are one of the most viable solutions for displacement amplification of piezoelectric actuators. This research proposes a novel compliant mechanism with a unique structure that enhances its out-of-plane stiffness, making it more suitable and reliable for positioning devices. That makes it more applicable in positioning devices. This mechanism, unlike other simple amplifying mechanisms such as bridge-type, has a center platform, which is supported from two sides.

Meanwhile, an analytical method was developed to model the kinetostatic and dynamic behaviors of the mechanism, and the nonlinear behavior of piezo and compliant mechanisms have been identified through the PI model. The results of the kinetostatic and dynamic modeling have been validated with both experimental setup and FEM software (ANSYS). The analytical method can estimate the amplification ratio, input stiffness, and output stiffness of the mechanism with a deviation of approximately 9.5%, 2%, and 13%, respectively. Additionally, the resonant frequency obtained from the dynamic stiffness method differs by about 6% and 8% from FEM and experiment. Also, the hysteresis identification model closely matches the experimental hysteresis loop with an RSME of less than $2\mu m$ for different frequencies. The overall results demonstrate that the analytical method and hysteresis identification could calculate the key factors of the mechanism and predict the behavior of the system. These results demonstrate that the validated analytical and hysteresis identification methods effectively predict the mechanism's behavior, providing a foundation for future work to optimize critical features such as natural frequency, input stiffness, output stiffness and amplification ratio.

## References


[1] D. Soleymanzadeh, H. Ghafarirad, M. Zareinejad, Sensorless adaptive sliding mode position control for piezoelectric actuators with charge leakage, Journal of Intelligent Material Systems and Structures, 31(1) (2020) 40-52.

[2] T.K. Das, B. Shirinzadeh, M. Ghafarian, A. Al-Jodah, Design, analysis, and experimental investigation of a single-stage and low parasitic motion piezoelectric actuated microgripper, Smart Materials and Structures, 29(4) (2020) 045028.

[3] W.L. Zhu, Z. Zhu, S. To, Q. Liu, B.F. Ju, X. Zhou, Redundantly piezo-actuated XYθz compliant mechanism for nano-positioning featuring simple kinematics, bi-directional motion and enlarged workspace, Smart Materials and Structures, 25(12) (2016) 125002.

[4] R. Hosseini, M. Hamedi, H. Golparvar, O. Zargar, Analytical and experimental investigation into increasing operating bandwidth of piezoelectric energy harvesters, AUT Journal of Mechanical Engineering, 3(1) (2019) 113-122.

[5] K. Mauser, M. Sjarov, A. Nowak, L.F. Campanile, A. Hasse, Design and control of actively prestressed compliant mechanisms for variable stiffness actuators, Journal of Intelligent Material Systems and Structures, 33(19) (2022) 2422-2439.

[6] V. Paniselvam, N.Y. Jin Tan, S.K. Anantharajan, A Review on the Design and Application of Compliant Mechanism-Based Fast-Tool Servos for Ultraprecision Machining, Machines, 11(4) (2023) 450.

[7] L. Zhao, X. Yu, P. Li, Y. Qiao, High-precision compliant mechanism for lens XY micro-adjustment, Review of Scientific Instruments, 91(3) (2020) 035004

[8] M. Ling, J. Cao, Z. Jiang, J. Lin, A semi-analytical modeling method for the static and dynamic analysis of complex compliant mechanism, Precision Engineering, 52 (2018) 64-72.

[9] N. Xu, M. Dai, X. Zhou, Analysis and design of symmetric notch flexure hinges, Advances in Mechanical Engineering, 9(11) (2017) 1687814017734513.

[10] L.G. Salmon, D.B. Gunyan, J.M. Derderian, P.G. Opdahl, L.L. Howell, Use of the Pseudo-Rigid Body Model to Simplify the Description of Complliant Micro-Mechanisms, in, Transducer Research Foundation Inc. (TRF), 2021, pp. 136-139.

[11] B. Hargrove, A. Nastevska, M. Frecker, J. Jovanova, Pseudo rigid body model for a nonlinear folding compliant mechanism, Mechanism and Machine Theory, 176 (2022) 105017.

[12] Y.Q. Yu, L.L. Howell, C. Lusk, Y. Yue, M.G. He, Dynamic modeling of compliant mechanisms based on the pseudo-rigid-body model, Journal of Mechanical Design, Transactions of the ASME, 127(4) (2005) 760-765.

[13] N. Lobontiu, J.S.N. Paine, E. Garcia, M. Goldfarb, Design of symmetric conic-section flexure hinges based on closed-form compliance equations, Mechanism and machine theory, 37(5) (2002) 477-498.

[14] J.W. Ryu, D.-G. Gweon, K.S. Moon, Optimal design of a flexure hinge based XYφ wafer stage, Precision engineering, 21(1) (1997) 18-28.

[15] H.-Y. Kim, D.-H. Ahn, D.-G. Gweon, Development of a novel 3-degrees of freedom flexure based positioning system, Rev Sci Instrum, 83(5) (2012) 055114.

[16] M. Ling, X. He, M. Wu, L. Cao, Dynamic Design of a Novel High-Speed Piezoelectric Flow Control Valve Based on Compliant Mechanism, IEEE/ASME Transactions on Mechatronics, 27(6) (2022) 4942-4950.

[17] M. Ling, L. Yuan, Z. Luo, T. Huang, X. Zhang, Enhancing Dynamic Bandwidth of Amplified Piezoelectric Actuators by a Hybrid Lever and Bridge-Type Compliant Mechanism, Actuators, 11(5) (2022).

[18] M. Ling, C. Zhang, L. Chen, Optimized design of a compact multi-stage displacement amplification mechanism with enhanced efficiency, Precision Engineering, 77 (2022) 77-89.

[19] M. Ling, X. Zhang, J. Cao, Extended Dynamic Stiffness Model for Analyzing Flexure- Hinge Mechanisms With Lumped Compliance, Journal of Mechanical Design, Transactions of the ASME, 144(1) (2022) 013304.

[20] I.D. Mayergoyz, Mathematical models of hysteresis and their applications, Academic press, 2003.

[21] D. Hughes, J.T. Wen, Preisach modeling of piezoceramic and shape memory alloy hysteresis, Smart materials and structures, 6(3) (1997) 287.

[22] M.A. Krasnosel'skii, A.V. Pokrovskii, Systems with hysteresis, Springer Science & Business Media, 2012.

[23] J. Gan, X. Zhang, H. Wu, A generalized Prandtl-Ishlinskii model for characterizing the rate-independent and rate-dependent hysteresis of piezoelectric actuators, Review of Scientific Instruments, 87(3) (2016) 035002.

[24] A. Visintin, Differential models of hysteresis, Springer Science & Business Media, 2013.

[25] C.-M. Chen, Y.-C. Hsu, R.-F. Fung, System identification of a Scott–Russell amplifying mechanism with offset driven by a piezoelectric actuator, Applied Mathematical Modelling, 36(6) (2012) 2788-2802.

[26] S. Bashash, N. Jalili, Robust multiple frequency trajectory tracking control of piezoelectrically driven micro/nanopositioning systems, IEEE Transactions on Control Systems Technology, 15(5) (2007) 867-878.

[27] M. Ling, L.L. Howell, J. Cao, Z. Jiang, A pseudo-static model for dynamic analysis on frequency domain of distributed compliant mechanisms, Journal of Mechanisms and Robotics, 10(5) (2018) 051011.

[28] M. Ling, X. Zhang, Coupled dynamic modeling of piezo-actuated compliant mechanisms subjected to external loads, Mechanism and Machine Theory, 160 (2021) 104283.

[29] H. Ghafarirad, S.M. Rezaei, A. Abdullah, M. Zareinejad, M. Saadat, Observer-based sliding mode control with adaptive perturbation estimation for micropositioning actuators, Precision Engineering, 35(2) (2011) 271-281.

**HOW TO CITE THIS ARTICLE**

*A. Mojibi, P. Firuzy Rad, H.Ghafarirad, A. Taghvaeipour, Kinetostatic and Dynamic Analyses of Micro-Positioning Compliant Mechanism Equipped with Piezoelectric Actuator, AUT J. Mech Eng., 9(2) (2025) 179-194.*

**DOI:** 10.22060/ajme.2025.23439.6135